ACS APPLIED MATERIALS & INTERFACES

www.acsami.org

Research Article

Engineering Electromagnetic Hot-Spots in Nanoparticle Cluster Arrays on Reflective Substrates for Highly Sensitive Detection of (Bio)molecular Analytes

Rishabh Rastogi, Ekoue A. Dogbe Foli, Remi Vincent, Pierre-Michel Adam, and Sivashankar Krishnamoorthy*

Cite This: *ACS Appl. Mater. Interfaces* 2021, 13, 32653−32661

Read Online

ACCESS | Metrics & More | Article Recommendations | Supporting Information

ABSTRACT: Intense electromagnetic (EM) hot-spots arising at the junctions or gaps in plasmonic nanoparticle assemblies can drive ultrahigh sensitivity in molecular detection by surface-enhanced spectroscopies. Harnessing this potential however requires access to the confined physical space at the EM hot-spots, which is a challenge for larger analytes such as biomolecules. Here, we demonstrate self-assembly derived gold nanoparticle cluster arrays (NCAs) on gold substrates exhibiting controlled interparticle (<1 nm wide) and intercluster (<10 nm wide) hot-spots as highly promising in this direction. Sensitivity of the NCAs toward detection of small (<1 nm) or large (protein−receptor interactions) analytes in surface-enhanced Raman and metal-enhanced fluorescence assays is found to be strongly impacted by the size of the cluster and the presence of reflective substrates. Experiments supported by numerical simulations attribute the higher sensitivity to higher EM field enhancements at the hot-spots, as well as greater analyte leverage over EM hot-spots. The best-performing arrays could push the sensitivity down to picomolar detection limits for sub-nanometric organic analytes as well as large protein analytes. The investigation paves the way for rational design of plasmonic biosensors and highlights the unique capabilities of a molecular self-assembly approach toward catering to this objective.

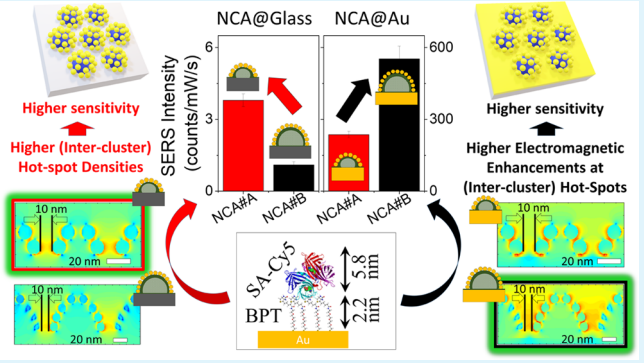

KEYWORDS: *electromagnetic hot-spot, surface-enhanced Raman spectroscopy, metal-enhanced fluorescence, plasmonic sensor, nanoparticle cluster, biosensor, self-assembly, colloidal assembly*

INTRODUCTION

Highly sensitive detection of molecular analytes is of strong importance to different sectors, including healthcare diagnostics, environmental monitoring, security, and space.[1−4] Nanoplasmonic sensors based on surface-enhanced spectroscopies, viz., surface-enhanced Raman spectroscopy (SERS) and metal-enhanced fluorescence (MEF), are particularly promising in this respect due to their ultralow detection limits within microscopic detection footprints and quick response times.[5] Nanoplasmonic sensors gain from high electromagnetic (EM) field enhancements arising at close vicinity to nanostructured metal surfaces. EM fields on plasmonic nanostructures exhibit spatial heterogeneity at the nanoscale, with significantly high EM enhancements at certain locations (hot-spots), such as sharp corners, or junctions in plasmonic nanoparticle (NP) assemblies. EM field enhancements at the hot-spots and analyte location with respect to the hot-spots are key determinants of the signal intensities in plasmon-enhanced spectroscopies.[6,7]

Advances in colloidal synthesis and nanolithography have shown to deliver a range of plasmonic nanoparticle assemblies exhibiting gap or curvature hot-spots.[8−13] Gap hot-spots provide a practical advantage over curvature hot-spots, as the interparticle gaps can be readily controlled by varying the density of nanoparticles on the surface.[14,15] Further, the sharp edges or corners are subject to instability due to erosion, breakage, or collapse. The EM enhancements at the gap hot-spots increase nonlinearly as a function of closing gap distances, resulting in EM enhancement factors over 10^8 for gaps of the order of a nanometer.[16,17] Despite high enhancements, the usefulness of such gap hot-spots for sensing of molecular analytes is restricted to analytes with dimensions

Received: January 29, 2021
Accepted: May 28, 2021
Published: July 9, 2021

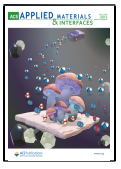

smaller than the gap distances. For larger analytes as encountered in bioassays, there is a nontrivial spatial trade-off to overcome, as the ultrasmall gaps are incompatible with the spatial needs to accommodate biomolecules and their receptors .

Different configurations have been explored in the literature to achieve analyte co-localization at EM gap hot-spots, including responsive structures,[18−21] mechanical instabilities,[22−25] and nanoparticles supported on metal thin films (MTFs).[26,27] Most of these configurations have been probed using small analytes, typically of sub-nanometric dimensions, e.g., molecules bound by thiol−gold interactions such as benzene thiol, dyes capable of resonance Raman effects such as rhodamine and crystal violet, and nonresonant, physisorbed analytes such as 2,2′-bipyridyl.[28−32] While such analytes are good to probe the EM enhancements of the plasmonic assemblies, they do not represent the challenge encountered in the sensing of large analytes such as biomolecules. Alternative approaches that include postformation of hot-spots after the analyte has been adsorbed on the surface, e.g., collapse of high-aspect-ratio metal nanopillars, do not permit rational design in the definition of the hot-spot geometry and are not compatible with multistep adsorption commonly used in bioassays.

Nanoparticles (NPs) on metal thin films (MTFs) are particularly interesting considering the ease of production of EM gap hot-spots without using complex lithographic tools. The optical response from NP−dielectric−MTF interfaces can be tuned by controlling the dielectric thickness,[33−37] nanoparticle size,[38] interparticle distance,[39] polarization and the incident angle,[40] or the choice of metal.[41] Hybridization between localized surface plasmons of NPs and delocalized surface plasmons from the metal thin film has been shown to result in EM enhancements at the NP−MTF gap and the interparticle gaps.[42] The localized EM fields at the NP−MTF gaps can be used to enhance sensitivity in detection of the analyte that can be accommodated at the gap.[40,43] In NP assemblies, strong interparticle plasmonic coupling at high NP density was found to result in a decrease in the EM field at NP−MTF gaps.[36] This was attributed to the increased scattering and absorption of incident light by the dense array of nanoparticles. The intense EM fields were achieved in any case at ultralow NP−MTF separations close to a nanometer, which is impractical to leverage for large biomolecular analytes.

Nanoparticles organized as clusters have shown to exhibit differential advantages compared to stochastic nanoparticle assemblies, viz., control over EM field profiles through the size and separation between nanoparticle clusters.[44,45] Yan et al. had earlier reported gold nanoparticle cluster arrays (NCAs) with controlled geometries to exhibit a strong dependence of SERS enhancement factors as a function of edge-to-edge separations of the clusters down to 50 nm.[44] The clusters were fabricated by electron-beam lithography, and the study reported a loss of pattern integrity for edge separations below 50 nm. In a subsequent study, we had demonstrated cluster arrays with edge-to-edge separations further reduced to 10 nm, leveraging self-assembly of block copolymer colloids.[45] Our study had shown further improvements to SERS sensitivity of organic molecules with sub-nanometric dimensions, as well as high uniformity in SERS spectra over areas spanning several square millimeters.[46,47] However, these investigations do not take advantage of the unique opportunities offered by hierarchical nanoparticle assemblies to produce hot-spots that can be efficiently leveraged for sensing of larger bioanalytes. In the current study, we demonstrate gold nanoparticle cluster arrays on gold thin films, with cluster dimensions that are engineered to drive high EM field enhancements at intercluster hot-spots. The intercluster hot-spots are large enough to accommodate large biomolecular interactions and are effectively leveraged within plasmon-enhanced spectroscopic bioassays. The sensitivity of SERS and MEF bioassays is shown to strongly correlate with the relative impact of gold over the glass substrate on the EM enhancements at the hot-spots, the relative densities of interparticle and intercluster EM hot-spots, and the relative dimensions of analyte with respect to these hot-spots. The tools of molecular self-assembly toward delivering well-defined cluster arrays while permitting orthogonal control over geometric variables are found to be critical to the investigation.

MATERIALS AND METHODS

Materials. Polystyrene-*block*-poly(2-vinylpyridine) (PS-*b*-PVP) (81.5 and 443 kDa) was purchased from Polymer Source Inc. (Montreal, Canada). Fused silica substrates were purchased from Siegert Wafer (Aachen, Germany). 1-Napthalenethiol (≥99%), *m*-xylene (≥99%), sodium citrate dihydrate (≥99%), and hydrogen tetrachloroaurate(III) trihydrate ($HAuCl_4 \cdot 3H_2O$) (≥99.9%) were purchased from Sigma-Aldrich. Biotin-PEG-thiols (BPTs) (400 g mol^{-1}) were purchased from Nanocs, New York. Phosphate buffer saline (PBS) and bovine serum albumin (BSA) solution were purchased from R&D Systems, Abingdon, U.K. Streptavidin conjugated with cyanine-5 dye (60 kDa) was purchased from Rockland, Limerick, PA. Supersharp, atomic force microscopy (AFM) tips (SSS−NCHR-50) were purchased from Nano and More (Paris, France).

Fabrication of Nanoparticle Cluster Arrays (NCAs). NCA#A and NCA#B were produced on fused silica or gold substrates using templates #A and #B produced from PS-*b*-P2VP with molecular weights of 81.5 kDa (polymer#A) and 443 kDa (polymer#B), respectively. Gold substrates were produced by coating 5 nm chromium and 100 nm gold on fused silica substrates using an electron-beam evaporator. Freshly cleaned substrates were spin-coated at 5000 rpm with 0.75% w w^{-1} of polymer#A and 3000 rpm with 2% w w^{-1} of polymer#B in m-xylene. The sample coated with polymer#B was exposed to 30 s of oxygen plasma (RIE Plasmatherm 790 RIE) to ensure adequate clearance between the features. Both template samples were immersed in a gold nanoparticle (diameter = 10.3 ± 0.5 nm) suspension synthesized in-house using a method reported earlier[48] for 2 h. The samples were subsequently rinsed thoroughly and dried prior to 1-napthalenethiol (NT) or protein assays. Topography images were acquired through tapping mode AFM measurements using an Innova microscope (Bruker, Santa Barbara) and SEM using a Helios NanoLab 650 (FEI, Eindhoven, the Netherlands). Gaussian fit to diameters, heights, and periodicities from Nanoscope analysis for AFM images and ImageJ analysis for SEM images was performed to validate geometric features used for modeling.

Optical Spectroscopic Measurements. Optical absorbance measurements were performed using a QE Pro UV-Visible-Near IR spectrometer (Ocean Optics, Florida). The sample was illuminated with a white light source and polarized through a 50×/0.42 NA objective. The transmitted light was collected using a 0.28 NA/20× objective, 8% of which was directed to a charge-coupled device (CCD) camera using a beam splitter to visualize the area under investigation, with the remaining light sent to the spectrophotometer via a multimode optical fiber. Reflectance measurements were acquired using an Ocean optics MAYA 2000PRO spectrometer (Ocean Optics, Florida) connected to an optical microscope through a 10×/0.30 NA objective. The samples were illuminated using a white light source (Chiu technology Lumina F0-150-220 (Halogen 150 W/220 V)), and a planar gold film on a glass substrate of similar thickness was used as a reference (100%).

https://doi.org/10.1021/acsami.1c01953
ACS Appl. Mater. Interfaces 2021, 13, 32653−32661

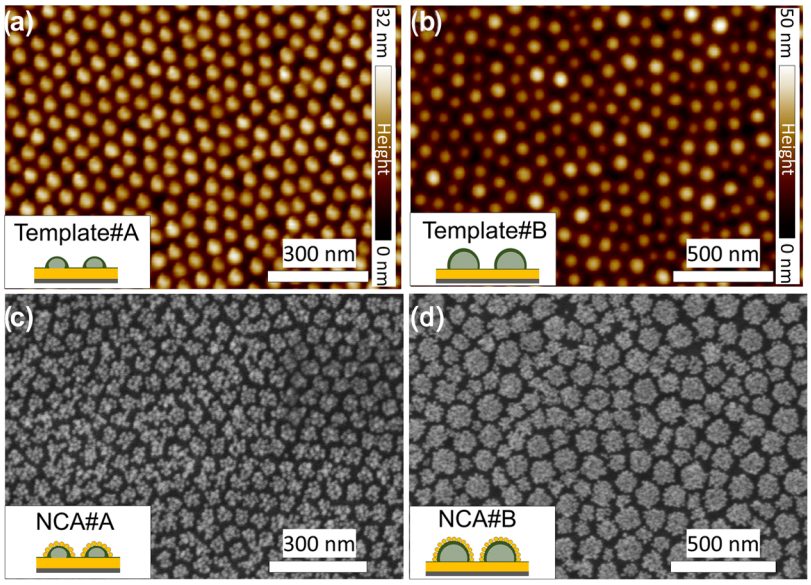

Figure 1. Geometric arrangement of the templates and the NCAs on gold substrates. AFM measurements of (a) Template#A and (b) Template#B. FESEM measurements of (c) NCA#A and (d) NCA#B. The schematic of the cross section of the templates and the NCAs are shown as insets.

SERS measurements were carried out using a micro-Raman system (Renishaw InVia, U.K.) attached with a microscope, a Peltier cooled CCD, and an excitation laser of 633 nm. The system was attached to a microscope (Leica) and a laser coupled through a 50×/0.5 NA objective. Before each experiment, internal silicon calibration was performed with a peak centered at 520 cm^{-1}. Data processing was performed using WIRE 5.0 software provided by the manufacturer of the system. Default parameters were used for baseline subtraction to remove the fluorescence background from the signals. All of the spectra were normalized with respect to exposure time and incident powers. For detection of 1-napthalenethiol, each measurement was acquired with a total exposure of 9 s at a laser power of 1.9 mW. For detection of the streptavidin−cyanine-5 (Cy5) conjugate, each measurement was acquired with 3 s of total exposure time at varying powers (1−5%) to prevent saturation of the CCD. The SERS spectra were obtained by subtraction of background fluorescence. In all cases, spectra were acquired in at least 10 different spots that were several millimeters apart, and the standard deviation of the spectral intensities of characteristic peaks are presented in the plots. The stability of the NCA samples in ethanol and PBS was assured through morphological characterization of the arrays using AFM and field emission scanning electron microscopy (FESEM) before and after exposure for at least 3 h.

Numerical Simulations. Numerical simulations were performed using the finite-difference time-domain (FDTD) method and a commercial software package from Lumericals Solution, Inc (Vancouver, Canada). A perfectly matched substrate layer was considered with a periodic boundary condition at the sides. Mesh sizes of dx = 0.1 nm, dy = 0.1 nm, dz = 0.4 nm were chosen after convergence analysis. An unpolarized excitation wavelength of 633 nm was used at normal incidence through the air medium. The simulated models were constructed by matching the best possible arrangements as measured from AFM and SEM images. NCA#A and NCA#B were modeled by distributing 12 or 48 nanoparticles (taken as gold nanospheres with material data from Olmon et al.),[49] respectively, with a nanoparticle diameter of 11.5 nm distributed in layers (two layers for A and four layers for B) around the features of template#A and template#B. The geometric parameters used for the models and their comparison with the experimental values are provided in the Supporting Information (Table S1).

Plasmonic Assays. For NT assays, the NCAs were immersed in an ethanolic solution of NT with different concentrations (μM to pM range) overnight and subsequently washed with ethanol and dried before SERS measurements. For protein assays, the NCAs were functionalized with an aqueous solution of biotin-PEG-thiol at 1 mM concentration for 2 h, followed by 30 min of 1% BSA in PBS and subsequently to different concentrations of SA-Cy5 in PBS. Exposure to the protein solutions was carried out within PDMS wells with a diameter and a height of 5 mm. The substrate was rinsed with PBS between each step. The calculation of the limit of detection (LOD = LOB + 1.645 [$SD_{low\ concentration}$]) was performed considering the limit of the blank (LOB = [$mean_{blank}$] + 1.645 [SD_{blank}]).[50]

RESULTS AND DISCUSSION

Nanoparticle Cluster Arrays (NCAs) on Gold Films. NCAs were fabricated on gold thin films by directed electrostatic attachment of negatively charged gold nanoparticles on self-organized polycationic block copolymer features, as we had reported earlier.[45] The process involves spin-coating solutions of polystyrene-*block*-polyvinylpyridine (PS-*b*-PVP) in an apolar solvent to obtain an ordered array of reverse micelle templates on the desired substrates. The geometric attributes of the templates can be controlled in steps of few nanometers by choice of the molecular weight of the copolymer, the solvent quality, solution concentration, and coating speeds.[8,45,51] The templates are scalable with high uniformity on arbitrarily large areas, such as full-wafers.[8,51] Upon exposure to an aqueous suspension of gold nanoparticles at mildly acidic or neutral pH, the PVP groups in the template are protonated, driving spatially selective electrostatic attachment of nanoparticles.[45] The resulting NCAs retain periodic organization of the original templates, with the size of the clusters (or the number of nanoparticles per cluster) defined by the surface area of the template features.

To investigate the impact of the size of clusters on optical properties, NCAs with two different cluster dimensions, NCA#A and NCA#B, were fabricated using templates#A and B derived from PS-*b*-P2VP with molecular weights of 81.5 and 443 kDa, respectively. The templates were produced by coating reverse micelles of the polymers from *m*-xylene solutions onto gold substrates (Figure 1a,b). The templates were exposed to an aqueous suspension consisting of gold nanoparticles with an average particle diameter of 10.3 nm at pH 6.8 to form NCAs (Figure 1c,d). The resulting NCAs

https://doi.org/10.1021/acsami.1c01953
ACS Appl. Mater. Interfaces 2021, 13, 32653−32661

exhibit an average of 11 and 42 nanoparticles per cluster for NCA#A and NCA#B, respectively (Figure S1, Supporting Information).

For the purpose of this investigation, NCAs with constant intercluster separations were prepared to ensure that the cluster size remains the only geometric variable under consideration. This measure enables attributing the differences in optical and spectroscopic responses to the difference in the size of the cluster. The intercluster separation was conserved between NCA#A and NCA#B between the NCAs as arising predominantly at 10 nm (histograms in Figure S2 a,b, Supporting Information) by controlling the pitch of the templates. The pitch could be controlled in steps of few nanometers by varying spin-coating speeds, as in our earlier publications.[45,51] To evaluate the role of the underlying substrate, control samples with NCA#A and NCA#B were prepared on fused silica substrates. The geometric attributes of templates A and B and those of the resulting NCAs were characterized using AFM and SEM and were found to vary <5% between the two substrates (Figures S3 and S4, Supporting Information). As a result, the NCAs on glass were found to exhibit intercluster separations equivalent to that of NCAs on gold (histograms in Figure S2 c,d). Attaining geometrically equivalent NCAs on glass (NCA@glass) and gold substrates (NCA@gold) assures the ability to separate the impact of the substrate from that of the NCA geometry while investigating the differences in optical and spectroscopic responses between NCA@glass and NCA@gold.

Optical Properties of NCAs. Optical properties of NCAs were investigated using absorbance spectra in the case of NCA@glass and reflectance spectra in the case of NCA@gold (Figure 2). The absorbance spectra of NCA@glass show a peak at 648 nm for NCA#A and 646 nm for NCA#B (Figure 2a). The reflectance spectra of NCA@glass present a dip at 647 nm for NCA#A and 669 nm for NCA#B (Figure 2b). The strongly red-shifted plasmon resonance peaks for NCAs as compared to isolated gold NPs (~520 nm) can be attributed in part to the strong interparticle and intercluster plasmonic coupling in the NCAs. This is further confirmed from EM field maps obtained by numerical simulations based on the finite-difference time-domain (FDTD) method at 633 nm excitation. The simulations rely on geometric models of NCAs constructed out of experimentally determined values for height, width, and density of the features on the template, the size of the gold nanoparticles, and the number of particles per cluster, as determined from AFM and SEM measurements (Table S1 and Figure S5, Supporting Information).

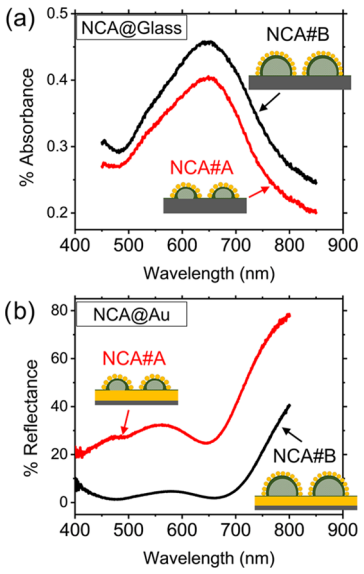

Figure 2. Comparison of optical response of NCAs on glass and gold substrates. (a) Absorbance spectra of NCAs on glass substrates, expressed as % absorbance with respect to the bare glass substrate and (b) reflectance spectra of NCAs on gold substrates, expressed as % reflectance with respect to the planar gold films.

EM field profiles of NCA reveal interparticle and intercluster hot-spots, with EM enhancements strongly dependent on the choice of the underlying substrate and the size of clusters. NCA@gold were found to exhibit greater EM field enhancements in interparticle and intercluster hot-spots as compared to NCA@glass (Figure 3). The higher EM enhancements

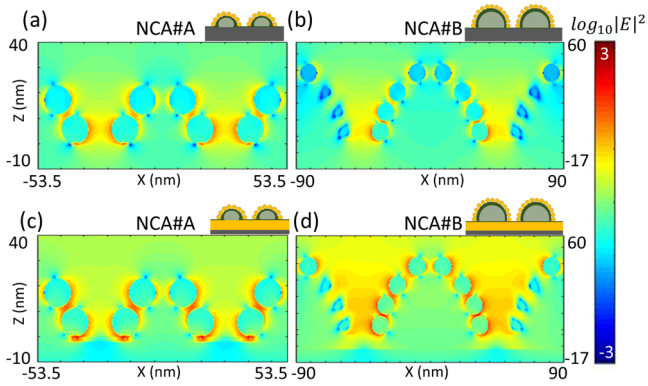

Figure 3. Simulated electromagnetic field maps at 633 nm of (a, c) NCA#A and (b, d) NCA#B supported on (a, b) glass and (c, d) gold substrates.

found in NCA@gold can be attributed to the role of the underlying gold film in increasing the field strength close to the cluster arrays. The strong localized field strength close to NCA@gold observed in the EM field maps at 633 nm corroborates with the observed dip in reflectance spectra at this wavelength. Unlike NCA@glass, (Figure 3 a,b) the EM enhancements in the case of NCA@gold (Figure 3 c,d) were found to be distinctly higher at interparticle hot-spots as compared to intercluster hot-spots.

Further, in the case of NCA@gold, the EM enhancements at the intercluster hot-spots are found to be greater for NCA#B as compared to NCA#A (Figure 3c,d), which indicates a stronger intercluster plasmonic coupling in NCA#B. This corroborates with the appearance of the reflectance dip at higher wavelengths in the case of NCA#B as compared to NCA#A (Figure 2b). In comparison, in the case of NCA@glass, the intercluster EM enhancements are found to be similar for NCA#A and NCA#B (Figure 3a,b). This implies a similar intercluster coupling irrespective of the cluster size, which corroborates with the observation of closely separated absorbance peak positions of NCA#A and NCA#B on glass substrates (Figure 2a). The field maps for NCA#B in case of NCA@gold (Figure 3d) show intercluster EM enhancement spanning a vertical distance of ~35 nm from the surface, which is approximately three-quarters of the height of the cluster. This is valuable considering that the EM enhancements at the hot-spot spans vertical space that is large enough to

https://doi.org/10.1021/acsami.1c01953
ACS Appl. Mater. Interfaces 2021, 13, 32653−32661

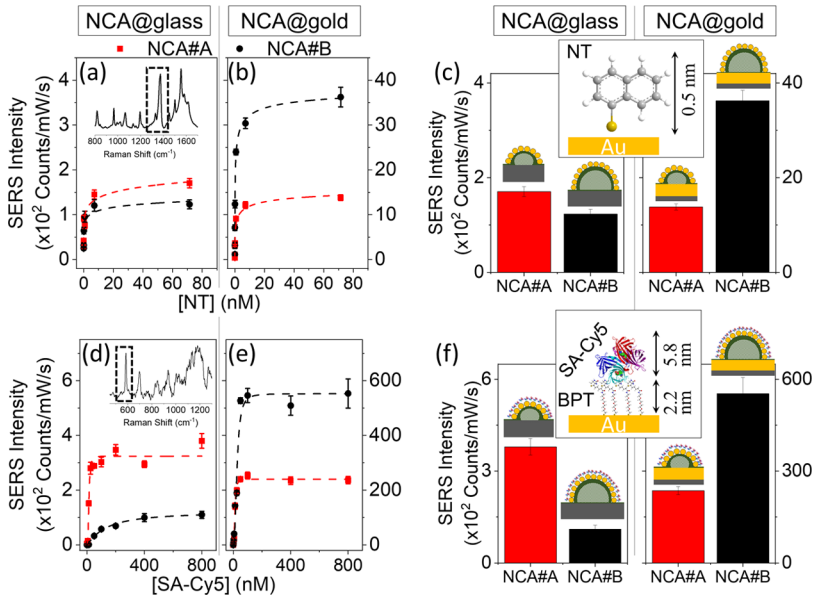

Figure 4. SERS assays of (a–c) NT on NCAs and (d–f) SA-Cy5 on biotinylated NCAs compared for NCA#A and NCA#B for NCA@glass and NCA@gold, respectively. (inset of a,d) The SERS spectra of NT and SA-Cy5 are shown, with the characteristic peaks used for the assays indicated by dashed lines (cf. Figure S6 in the Supporting Information for SERS spectra for all concentrations). (c, f) Bar plots comparing SERS signal intensities at saturated densities of NT and SA-Cy5. The molecular structure and dimensions for NT and SA-Cy5 are shown as insets.

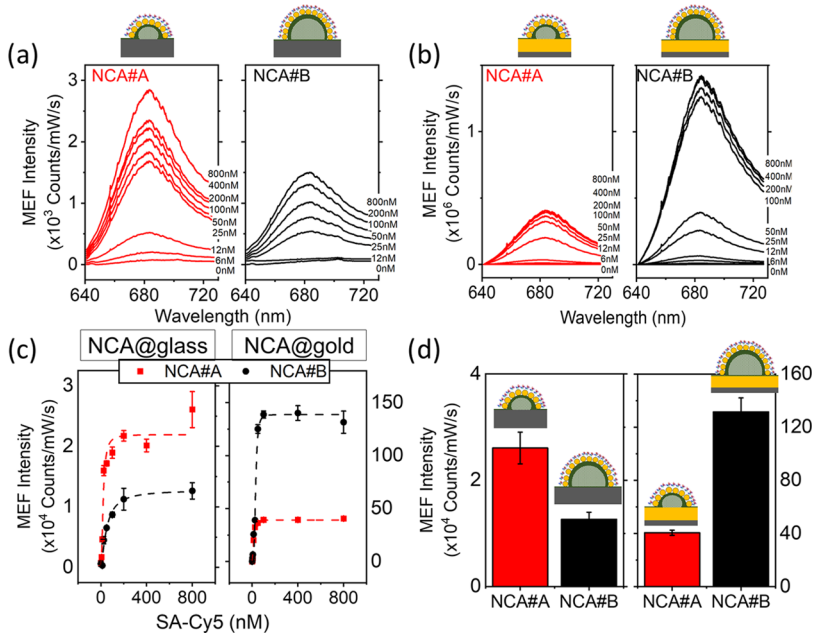

Figure 5. Evolution of MEF spectra as a function of the concentration of SA-Cy5 on biotinylated NCAs compared for (a, b, left panel) NCA#A and (a, b, right panel) NCA#B for (a) NCA@glass and (b) NCA@gold. (c) MEF assays for (left) NCA@glass and (right) NCA@gold. (d) Comparison of maximum MEF signal intensities of SA-Cy5 on NCA#A and NCA#B compared for NCA@glass and NCA@gold.

accommodate the interaction dimensions of most common biological interactions, e.g., immunosandwich assays or hybridization of nucleic acid sequences.

Plasmon-Enhanced Spectroscopic Assays. The sensitivity of NCA@gold toward detection of molecular analytes was tested using surface-enhanced Raman spectroscopy (SERS) at 633 nm excitation (Figure 4). SERS assays were performed for two different molecules, 1-napthalenethiol (NT) and streptavidin labeled with cyanine-5 (Cy5), with dimensions that were an order of magnitude apart (insets in Figure 4c,f). NT was chosen on the basis of its ultrasmall size <1 nm and its ease in forming a conformal self-assembled monolayer on a gold nanoparticle surface. The sub-nanometric dimensions of NT allow it to access and leverage both interparticle and intercluster EM hot-spots in the NCAs. The choice of SA-Cy5 was made on the basis of its well-studied and high-affinity interaction with biotin.[52,53] The binding of SA-Cy5 to the biotinylated NCA surface represents the simplest case of receptor–ligand interaction used in bioassays. NCAs are easily biotinylated using self-assembled monolayers of biotin-PEG-thiols (BPTs) to render them specific to the binding of SA-Cy5. The dimensions of BPTs (~2.2 nm) and

https://doi.org/10.1021/acsami.1c01953
ACS Appl. Mater. Interfaces 2021, 13, 32653–32661

SA-Cy5 (5.8 nm) render the pair too large to be accommodated in interparticle hot-spots but accommodated easily enough in the intercluster hot-spots. Further, the choice of Cy5 as a label can help signal enhancements due to resonance Raman effect arising from the alignment of the excitation wavelength with the molecular absorbance of Cy5.[54]

The sensitivity of the NCAs toward detection of NT was tested by following the intensity of the characteristic vibrational Raman bands of NT at 1372 cm^{-1} as a function of the NT solution concentration between 0.07 nM and 71.5 μM (Figure 4a inset, Figure S6a,b in Supporting Information). The assays of SA-Cy5 were performed by biotinylated NCA, by following the intensity of the characteristic Raman band of Cy5 at 583 cm^{-1} between 0.1 and 800 nM[54] (Figure 4d inset, Figure S6c,d in Supporting Information). The assays were performed under identical conditions for both NCA@gold and NCA@glass samples. The SERS signal intensities were found to be higher for NCA@gold as compared to those of NCA@glass by at least an order of magnitude for NT assays (Figure 4a−c) and at least 2 orders of magnitude in the case of SA-Cy5 assays (Figure 4d−f). A significant difference in sensitivities was observed for both analytes depending on the size of the clusters, and the choice of the substrate. In the case of NCA@gold, NCA#B shows higher sensitivity compared to NCA#A for both NT and SA-Cy5 (Figure 4b,e,c,f). However, the NCA@glass samples exhibited the opposite trend, with NCA#A exhibiting distinctly higher sensitivity toward SA-Cy5 and similar sensitivities toward NT as compared to NCA#B (Figure 4a,d,c,f). NCA#B on gold was thus found to be most sensitive in the SERS assays. An estimation of the lowest limit of detection (LOD) shows the sensitivity of NCA#B down to 600 pM in the case of NT and 400 pM in the case of SA-Cy5 assays. In comparison, the LOD in the case of NCA#A, which performed better on glass substrates, was found to be 6.8 nM for NT and 2 nM for SA-Cy5.

The use of Cy5 as label allows detection of SA-Cy5 using Raman and fluorescence spectroscopies. The strong plasmonic enhancement of EM fields close to NCA is expected to result in a strong enhancement of fluorescence signals from Cy5 due to metal-enhanced fluorescence (MEF).[55−57] For MEF to occur, the fluorophore is expected to be separated from the metal surface to avoid fluorescence quenching due to direct fluorophore−metal contact. The presence of a BPT monolayer with a thickness of 2.2 nm can satisfy this requirement. Results show strong enhancement of Cy5 fluorescence on NCAs, with the signal intensities on NCA@gold to be ∼2 orders of magnitude greater than those on NCA@glass (Figure 5). Further, as observed in the case of SERS assays, MEF signal intensities were also found to be higher for NCA#B than NCA#A on gold substrates (Figure 5b, right panel of c,d) and higher for NCA#A than NCA#B on glass substrates (Figure 5a, left panel of c,d). The signal intensities were found to be the highest for NCA#B, for the entire concentration range, in all cases. The MEF assays on NCA#B on gold were found to exhibit a LOD of 400 pM, which is the same as that observed for the SERS assays. NCA#A, which is more sensitive on glass, was found to exhibit a LOD of 6.2 nM, which is over an order of magnitude higher than that of NCA#B on gold.

The trends in sensitivity observed in the SERS and MEF assays for NCA@gold as compared to NCA@glass are strongly aligned to expectations set by the EM field profiles obtained from numerical simulations. Overall, NCA@gold clearly resulted in high signal-intensity enhancements compared to NCA@glass for both NT and SA-Cy5. This agrees with the higher EM enhancements at the interparticle and intercluster EM hot-spots as observed in simulated EM field maps of NCA@gold (Figure 3c,d). The trends observed for signal-intensity enhancements for NT (Figure 4a−c) are found to corroborate with the simulated EM field profiles of interparticle EM hot-spots (Figure 3). For NCA@gold, NCA#B presents a higher density of interparticle EM hot-spots exhibiting high EM enhancements, which can explain the observed higher SERS signal intensities. For NCA@glass, the considerably less difference in observed SERS signal intensities for NT for both large and small clusters can be explained by the lack of significant difference in the EM enhancements at the interparticle hot-spots over intercluster hot-spots (Figure 3a,b). Since NT can leverage both these hot-spots, the lack of significant EM enhancement at the interparticle hot-spots reduces the advantage due to higher interparticle hot-spot densities in NCA#B on glass.

The higher signal intensities for SA-Cy5 observed on NCA#B on gold substrates are also found to corroborate with the greater intercluster EM enhancements observed in the EM field profiles of NCA#B (Figure 3d). The agreement between simulation and experiments supports the hypothesis that the intercluster EM enhancements are leveraged by SA-Cy5. In the case of NCA@glass samples, the intercluster EM field enhancements were found to be similar for both NCA#A and NCA#B (Figure 3a,b). However, NCA#A has a clear advantage due to the higher density of intercluster hot-spots, which is over three times greater than that of NCA#B (Figure S3). Given that SA-Cy5 could effectively leverage only the intercluster hot-spots, the greater number density of intercluster hot-spots in NCA#A renders it more sensitive in protein detection. This further indicates that in the case of NCA@gold, the signal contribution arising from greater intercluster EM enhancements in the case of NCA#B outweighs the advantage of higher intercluster hot-spot densities in NCA#A. Thus, the observed sensitivity of NCA for the two different analytes as a function of NCA geometry and the choice of substrate can be rationalized as a product of two major factors, viz., (a) EM field distribution as determined by the NCA geometry and the choice of substrate and (b) analyte access to EM hot-spots, as determined by the size of the analyte in relation to the interparticle and intercluster EM hot-spots.

Besides the performance in molecular sensing, there are other practical considerations that govern the user's choice between glass and gold substrates. Glass substrates are attractive for biological experiments due to their transparency that enables imaging using transmitted light illumination. Gold substrates, on the other hand, are invariably encountered while working with analytical tools such as surface plasmon resonance, quartz crystal microbalance, and surface acoustic wave devices. The current work provides rational guidance on the choice of cluster dimensions that enhance NCA sensitivity for a given substrate type while demonstrating larger clusters on gold substrates as a preferred choice when there are no constraints on the choice of substrate. The investigations further benefit from the high stability and the reproducibility of the NCAs, which are also aspects of practical importance for their deployment in molecular sensing applications. The NCAs on glass and gold substrates were stable in the aqueous and organic media used, viz., NT immobilization from ethanolic solutions and biological experiments under aqueous buffer.

https://doi.org/10.1021/acsami.1c01953
ACS Appl. Mater. Interfaces 2021, 13, 32653−32661

The excellent uniformity in spectral intensities from spectra acquired across the NCAs from spots separated by several millimeters is an observation that is strongly linked to uniformity in geometries of the self-assembled templates and the pattern-transfer steps to produce plasmonic arrays, as shown in our earlier reports.[8,46,51,58]

CONCLUSIONS

Gold nanoparticle cluster arrays (NCAs) exhibiting interparticle (<1 nm wide) and intercluster (~10 nm wide) hotspots were produced on glass and gold substrates and compared for their sensitivity toward quantitative detection of molecular analytes by SERS and MEF. The impact of NCA geometry on sensing performance was investigated while factoring in the impact of the EM enhancements at the hotspots, density of hot-spots, and the dimension of the analyte in relation to the hot-spots. The cluster size and densities that resulted in higher sensitivity were found to be dependent on the choice of substrate, viz., NCAs with larger clusters and lower densities (NCA#B) were more sensitive in the case of NCA@gold, while smaller clusters with higher densities (NCA#A) were found to be more sensitive in the case of NCA@glass. The NCA geometry that is more sensitive in each case was found to match the condition necessary to drive better leverage for the analyte over EM hot-spots. Studying the impact of the size of the analyte in relation to the dimensions of the hot-spots reveals the intercluster hot-spots to be better adapted to accommodate large biomolecular analytes. Higher sensitivity in SA-Cy5 assays was achieved for smaller clusters on glass due to a greater number of intercluster hot-spots and larger clusters on gold due to higher EM enhancements at the intercluster hot-spots. In all cases, the NCAs were found to be capable of quantitative detection of both sub-nanometric organic molecules and larger protein molecules, with sensitivity down to 600 pM (or 96 ppb) of NT and 400 pM (or 22 ng mL^{-1}) of SA-Cy5. The results inspire rational engineering of plasmonic nanoarrays to simultaneously drive high EM enhancements and analyte co-localization at the hot-spots. The use of molecular self-assembly is particularly well adapted to engineer such arrays, providing convenient handles for systematic and orthogonal control over geometric attributes down to molecular length scales, with scalability and throughput necessary to support large-scale investigations.

ASSOCIATED CONTENT

Supporting Information

The Supporting Information is available free of charge at https://pubs.acs.org/doi/10.1021/acsami.1c01953.

AFM of template geometries on glass and gold substrates; FESEM measurements of NCAs on glass and gold substrates; histograms of the number of particles per cluster for NCA#A and NCA#B; histograms of intercluster separations of both NCAs on glass and gold substrates; geometric values and schematic of the geometric model employed for FDTD simulations; and SERS spectral evolution at different concentrations shown for NT and SA-Cy5 (PDF)

AUTHOR INFORMATION

Corresponding Author

Sivashankar Krishnamoorthy − *MRT Department, Luxembourg Institute of Technology, Belvaux L-4422, Luxembourg;* orcid.org/0000-0003-0410-1696; Email: sivashankar.krishnamoorthy@list.lu

Authors

Rishabh Rastogi − *MRT Department, Luxembourg Institute of Technology, Belvaux L-4422, Luxembourg; Laboratory Light, Nanomaterials and Nanotechnologies-L2n, University of Technology of Troyes and CNRS ERL 7004, Troyes 10000, France;* orcid.org/0000-0003-3482-203X

Ekoue A. Dogbe Foli − *Laboratory Light, Nanomaterials and Nanotechnologies-L2n, University of Technology of Troyes and CNRS ERL 7004, Troyes 10000, France*

Remi Vincent − *Laboratory Light, Nanomaterials and Nanotechnologies-L2n, University of Technology of Troyes and CNRS ERL 7004, Troyes 10000, France*

Pierre-Michel Adam − *Laboratory Light, Nanomaterials and Nanotechnologies-L2n, University of Technology of Troyes and CNRS ERL 7004, Troyes 10000, France*

Complete contact information is available at: https://pubs.acs.org/10.1021/acsami.1c01953

Author Contributions

The manuscript was written through the contributions of all authors. All authors have given approval to the final version of the manuscript.

Notes

The authors declare no competing financial interest.

ACKNOWLEDGMENTS

Funding from National Research Funding Agency of Luxembourg (FNR) via projects PLASENS (C15/MS/10459961), VIRANOSTIC, and MASSENA is gratefully acknowledged. S.K. and R.R. acknowledge discussions and travel funding from EU COST Action BIONECA. E.A.D.F. and R.V. are thankful for the support of the Fonds Européen de développement économique et régional (FEDER) for the project LDOS.

ABBREVIATIONS

EM, electromagnetic
NCA, nanocluster arrays
SERS, surface-enhanced Raman spectroscopy
MEF, metal-enhanced fluorescence
FDTD, finite-difference time-domain
FESEM, field emission scanning electron microscopy
AFM, atomic force microscopy

REFERENCES

(1) Rusling, J. F.; Kumar, C. V.; Gutkind, J. S.; Patel, V. Measurement of Biomarker Proteins for Point-of-Care Early Detection and Monitoring of Cancer. *Analyst* **2010**, *135*, 2496−2511.
(2) Jain, K. K. Nanotechnology in Clinical Laboratory Diagnostics. *Clin. Chim. Acta* **2005**, *358*, 37−54.
(3) Wabuyele, M. B.; Martin, M. E.; Yan, F.; Stokes, D. L.; Mobley, J.; Cullum, B. M.; Wintenberg, A. L.; Lenarduzzi, R.; Vo-Dinh, T. Portable Raman Integrated Tunable Sensor (RAMiTs) for Environmental Field Monitoring. In *Advanced Environmental, Chemical, and Biological Sensing Technologies II*; International Society for Optics and Photonics, 2004; Vol. *5586*, p 60.
(4) Spencer, K. M.; Sylvia, J. M.; Marren, P. J.; Bertone, J. F.; Christesen, S. D. Surface-Enhanced Raman Spectroscopy for Homeland Defense. In *Chemical and Biological Point Sensors for Homeland Defense*; International Society for Optics and Photonics, 2004; Vol. *5269*.

(5) Mun, J.; Lee, D.; So, S.; Badloe, T.; Rho, J. Surface-Enhanced Spectroscopy: Toward Practical Analysis Probe. *Appl. Spectrosc. Rev.* **2019**, *54*, 142−175.
(6) Fang, Y.; Seong, N. H.; Dlott, D. D. Measurement of the Distribution of Site Enhancements in Surface-Enhanced Raman Scattering. *Science* **2008**, *321*, 388−392.
(7) Benz, F.; Tserkezis, C.; Herrmann, L. O.; de Nijs, B.; Sanders, A.; Sigle, D. O.; Pukenas, L.; Evans, S. D.; Aizpurua, J.; Baumberg, J. J. Nanooptics of Molecular-Shunted Plasmonic Nanojunctions. *Nano Lett.* **2015**, *15*, 669−674.
(8) Rastogi, R.; Beggiato, M.; Adam, P. M.; Juodkazis, S.; Krishnamoorthy, S. Nanoplasmonic Arrays with High Spatial Resolutions, Quality, and Throughput for Quantitative Detection of Molecular Analytes. In *Nanoplasmonics*; IntechOpen, 2019.
(9) Grillet, N.; Manchon, D.; Bertorelle, F.; Bonnet, C.; Broyer, M.; Cottancin, E.; Lermé, J.; Hillenkamp, M.; Pellarin, M. Plasmon Coupling in Silver Nanocube Dimers: Resonance Splitting Induced by Edge Rounding. *ACS Nano* **2011**, *5*, 9450−9462.
(10) Guerrini, L.; Graham, D. Molecularly-Mediated Assemblies of Plasmonic Nanoparticles for Surface-Enhanced Raman Spectroscopy Applications. *Chem. Soc. Rev.* **2012**, *41*, 7085−7107.
(11) Chen, S.-Y.; Lazarides, A. A. Quantitative Amplification of Surface Enhanced Raman Scattering through Plasmonic Coupling in Controlled Nanoparticle Assemblies. In *Plasmonics: Nanoimaging, Nanofabrication, and their Applications V*; International Society for Optics and Photonics, 2009; Vol. *7395*, p 73951S.
(12) Wang, Q.; Wang, Z.; Li, Z.; Xiao, J.; Shan, H.; Fang, Z.; Qi, L. Controlled Growth and Shape-Directed Self-Assembly of Gold Nanoarrows. *Sci. Adv.* **2017**, *3*, No. e1701183.
(13) Krishnamoorthy, S.; Hinderling, C.; Heinzelmann, H. Nanoscale Patterning with Block Copolymers. *Mater. Today* **2006**, *9*, 40−47.
(14) Kim, M.; Kwon, H.; Lee, S.; Yoon, S. Effect of Nanogap Morphology on Plasmon Coupling. *ACS Nano* **2019**, *13*, 12109−12119.
(15) Esteban, R.; Aguirregabiria, G.; Borisov, A. G.; Wang, Y. M.; Nordlander, P.; Bryant, G. W.; Aizpurua, J. The Morphology of Narrow Gaps Modifies the Plasmonic Response. *ACS Photonics* **2015**, *2*, 295−305.
(16) Nie, S.; Emory, S. R. Probing Single Molecules and Single Nanoparticles by Surface-Enhanced Raman Scattering. *Science* **1997**, *275*, 1102−1106.
(17) Le Ru, E. C.; Blackie, E.; Meyer, M.; Etchegoin, P. G. Surface Enhanced Raman Scattering Enhancement Factors: A Comprehensive Study. *J. Phys. Chem. C* **2007**, *111*, 13794−13803.
(18) Wang, T.; Yu, Y.; Chen, D.; Wang, S.; Zhang, X.; Li, Y.; Zhang, J.; Fu, Y. Naked Eye Plasmonic Indicator with Multi-Responsive Polymer Brush as Signal Transducer and Amplifier. *Nanoscale* **2017**, *9*, 1925−1933.
(19) Zheng, Y.; Soeriyadi, A. H.; Rosa, L.; Ng, S. H.; Bach, U.; Justin Gooding, J. Reversible Gating of Smart Plasmonic Molecular Traps Using Thermoresponsive Polymers for Single-Molecule Detection. *Nat. Commun.* **2015**, *6*, No. 8797.
(20) Drachev, V. P.; Shalaev, V. M. Biomolecule Sensing with Adaptive Plasmonic Nanostructures. *Surf. Enhanced Raman Scattering* **2006**, *366*, 351−366.
(21) Drachev, V. P.; Thoreson, M. D.; Nashine, V.; Khaliullin, E. N.; Ben-Amotz, D.; Davisson, V. J.; Shalaev, V. M. Adaptive Silver Films for Surface-Enhanced Raman Spectroscopy of Biomolecules. *J. Raman Spectrosc.* **2005**, *36*, 648−656.
(22) Chandra, D.; Yang, S. Capillary-Force-Induced Clustering of Micropillar Arrays: Is It Caused by Isolated Capillary Bridges or by the Lateral Capillary Meniscus Interaction Force? *Langmuir* **2009**, *25*, 10430−10434.
(23) Kim, A.; Ou, F. S.; Ohlberg, D. A. A.; Hu, M.; Williams, R. S.; Li, Z. Study of Molecular Trapping inside Gold Nanofinger Arrays on Surface-Enhanced Raman Substrates. *J. Am. Chem. Soc.* **2011**, *133*, 8234−8239.
(24) Lee, S. J.; Morrill, A. R.; Moskovits, M. Hot Spots in Silver Nanowire Bundles for Surface-Enhanced Raman Spectroscopy. *J. Am. Chem. Soc.* **2006**, *128*, 2200−2201.
(25) Schmidt, M. S.; Hübner, J.; Boisen, A. Large Area Fabrication of Leaning Silicon Nanopillars for Surface Enhanced Raman Spectroscopy. *Adv. Mater.* **2012**, *24*, OP11−OP18.
(26) Chikkaraddy, R.; Turek, V. A.; Kongsuwan, N.; Benz, F.; Carnegie, C.; Van De Goor, T.; De Nijs, B.; Demetriadou, A.; Hess, O.; Keyser, U. F.; et al. Mapping Nanoscale Hotspots with Single-Molecule Emitters Assembled into Plasmonic Nanocavities Using DNA Origami. *Nano Lett.* **2018**, *18*, 405−411.
(27) Li, A.; Isaacs, S.; Abdulhalim, I.; Li, S. Ultrahigh Enhancement of Electromagnetic Fields by Exciting Localized with Extended Surface Plasmons. *J. Phys. Chem. C* **2015**, *119*, 19382−19389.
(28) Bell, S. E. J.; Charron, G.; Cortés, E.; Kneipp, J.; de la Chapelle, M. L.; Langer, J.; Procházka, M.; Tran, V.; Schlücker, S. Towards Reliable and Quantitative Surface-Enhanced Raman Scattering (SERS): From Key Parameters to Good Analytical Practice. *Angew. Chem., Int. Ed.* **2020**, *59*, 5454−5462.
(29) Kleinman, S. L.; Ringe, E.; Valley, N.; Wustholz, K. L.; Phillips, E.; Scheidt, K. A.; Schatz, G. C.; Van Duyne, R. P. Single-Molecule Surface-Enhanced Raman Spectroscopy of Crystal Violet Isotopologues: Theory and Experiment. *J. Am. Chem. Soc.* **2011**, *133*, 4115−4122.
(30) Dinda, S.; Yap, F. L.; Suresh, V.; Gupta, R. K.; Das, D.; Krishnamoorthy, S. Quantitative Detection with Surface Enhanced Raman Scattering (SERS) Using Self-Assembled Gold Nanoparticle Cluster Arrays. *Aust. J. Chem.* **2013**, *66*, 1034−1038.
(31) Muehlethaler, C.; Leona, M.; Lombardi, J. R. Towards a Validation of Surface-Enhanced Raman Scattering (SERS) for Use in Forensic Science: Repeatability and Reproducibility Experiments. *Forensic Sci. Int.* **2016**, *268*, 1−13.
(32) Zhang, K.; Zeng, T.; Tan, X.; Wu, W.; Tang, Y.; Zhang, H. A Facile Surface-Enhanced Raman Scattering (SERS) Detection of Rhodamine 6G and Crystal Violet Using Au Nanoparticle Substrates. *Appl. Surf. Sci.* **2015**, *347*, 569−573.
(33) Mock, J. J.; Hill, R. T.; Degiron, A.; Zauscher, S.; Chilkoti, A.; Smith, D. R. Distance-Dependent Plasmon Resonant Coupling between a Gold Nanoparticle and Gold Film. *Nano Lett.* **2008**, *8*, 2245−2252.
(34) Ciracì, C.; Hill, R. T.; Mock, J. J.; Urzhumov, Y.; Fernández-Domínguez, A. I.; Maier, S. A.; Pendry, J. B.; Chilkoti, A.; Smith, D. R. Probing the Ultimate Limits of Plasmonic Enhancement. *Science* **2012**, *337*, 1072−1074.
(35) Hu, M.; Ghoshal, A.; Marquez, M.; Kik, P. G. Single Particle Spectroscopy Study of Metal-Film-Induced Tuning of Silver Nanoparticle Plasmon Resonances. *J. Phys. Chem. C* **2010**, *114*, 7509−7514.
(36) Li, A.; Srivastava, S. K.; Abdulhalim, I.; Li, S. Engineering the Hot Spots in Squared Arrays of Gold Nanoparticles on a Silver Film. *Nanoscale* **2016**, *8*, 15658−15664.
(37) He, L.; Smith, E. A.; Natan, M. J.; Keating, C. D. The Distance-Dependence of Colloidal Au-Amplified Surface Plasmon Resonance. *J. Phys. Chem. B* **2004**, *108*, 10973−10980.
(38) Chu, Y.; Crozier, K. B. Experimental Study of the Interaction between Localized and Propagating Surface Plasmons. *Opt. Lett.* **2009**, *34*, No. 244.
(39) Srivastava, S. K.; Li, A.; Li, S.; Abdulhalim, I. Optimal Interparticle Gap for Ultrahigh Field Enhancement by LSP Excitation via ESPs and Confirmation Using SERS. *J. Phys. Chem. C* **2016**, *120*, 28735−28742.
(40) Mubeen, S.; Zhang, S.; Kim, N.; Lee, S.; Krämer, S.; Xu, H.; Moskovits, M. Plasmonic Properties of Gold Nanoparticles Separated from a Gold Mirror by an Ultrathin Oxide. *Nano Lett.* **2012**, *12*, 2088−2094.
(41) Kim, K.; Choi, J. Y.; Shin, K. S. Enhanced Raman Scattering in Gaps Formed by Planar Au and Au/Ag Alloy Nanoparticles. *J. Phys. Chem. C* **2013**, *117*, 11421−11427.

https://doi.org/10.1021/acsami.1c01953
ACS Appl. Mater. Interfaces 2021, 13, 32653−32661

(42) Maurer, T.; Adam, P. M.; Lévêque, G. Coupling between Plasmonic Films and Nanostructures: From Basics to Applications. *Nanophotonics* **2015**, *4*, 363−382.
(43) Dai, F.; Horrer, A.; Adam, P. M.; Fleischer, M. Accessing the Hotspots of Cavity Plasmon Modes in Vertical Metal−Insulator−Metal Structures for Surface Enhanced Raman Scattering. *Adv. Opt. Mater.* **2020**, *8*, No. 1901734.
(44) Yan, B.; Thubagere, A.; Premasiri, W. R.; Ziegler, L. D.; Dal Negro, L.; Reinhard, B. M. Engineered SERS Substrates with Multiscale Signal Enhancement: Nanoparticle Cluster Arrays. *ACS Nano* **2009**, *3*, 1190−1202.
(45) Yap, F. L.; Thoniyot, P.; Krishnan, S.; Krishnamoorthy, S. Nanoparticle Cluster Arrays for High-Performance SERS through Directed Self-Assembly on Flat Substrates and on Optical Fibers. *ACS Nano* **2012**, *6*, 2056−2070.
(46) Yap, F. L.; Thoniyot, P.; Krishnan, S.; Krishnamoorthy, S. Nanoparticle Cluster Arrays for High-Performance SERS through Directed Self-Assembly on Flat Substrates and on Optical Fibers. *ACS Nano* **2012**, *6*, 2056−2070.
(47) Dinda, S.; Yap, F. L.; Suresh, V.; Gupta, R. K.; Das, D.; Krishnamoorthy, S. Quantitative Detection with Surface Enhanced Raman Scattering (SERS) Using Self-Assembled Gold Nanoparticle Cluster Arrays. *Aust. J. Chem.* **2013**, *66*, 1034−1038.
(48) Plech, A.; Kimling, J.; Maier, M.; Okenve, B.; Kotaidis, V.; Ballot, H. Turkevich Method for Gold Nanoparticle Synthesis Revisited. *J. Phys. Chem. B* **2006**, *110*, 15700−15707.
(49) Olmon, R. L.; Slovick, B.; Johnson, T. W.; Shelton, D.; Oh, S. H.; Boreman, G. D.; Raschke, M. B. Optical Dielectric Function of Gold. *Phys. Rev. B: Condens. Matter Mater. Phys.* **2012**, *86*, No. 235147.
(50) Armbruster, D. A.; Pry, T. Limit of Blank, Limit of Detection and Limit of Quantitation. *Clin. Biochem. Rev.* **2008**, *29*, S49−S52.
(51) Krishnamoorthy, S.; Manipaddy, K. K.; Yap, F. L. Wafer-Level Self-Organized Copolymer Templates for Nanolithography with Sub-50 Nm Feature and Spatial Resolutions. *Adv. Funct. Mater.* **2011**, *21*, No. 1102.
(52) Wilchek, M.; Bayer, E. A.; Livnah, O. Essentials of Biorecognition: The (Strept)Avidin-Biotin System as a Model for Protein-Protein and Protein-Ligand Interaction. *Immunol. Lett.* **2006**, *103*, 27−32.
(53) Green, N. M. Avidin. *Adv. Protein Chem.* **1975**, *29*, 85−133.
(54) Mahajan, S.; Baumberg, J. J.; Russell, A. E.; Bartlett, P. N. Reproducible SERRS from Structured Gold Surfaces. *Phys. Chem. Chem. Phys.* **2007**, *9*, 6016−6020.
(55) Aslan, K.; Gryczynski, I.; Malicka, J.; Matveeva, E.; Lakowicz, J. R.; Geddes, C. D. Metal-Enhanced Fluorescence: An Emerging Tool in Biotechnology. *Curr. Opin. Biotechnol.* **2005**, *16*, 55−62.
(56) Fu, Y.; Lakowicz, J. R. Enhanced Fluorescence of Cy5-Labeled Oligonucleotides near Silver Island Films: A Distance Effect Study Using Single Molecule Spectroscopy. *J. Phys. Chem. B* **2006**, *110*, 22557−22562.
(57) Dragan, A. I.; Bishop, E. S.; Casas-Finet, J. R.; Strouse, R. J.; McGivney, J.; Schenerman, M. A.; Geddes, C. D. Distance Dependence of Metal-Enhanced Fluorescence. *Plasmonics* **2012**, *7*, 739−744.
(58) Rastogi, R.; Arianfard, H.; Moss, D.; Juodkazis, S.; Adam, P.-M.; Krishnamoorthy, S. Analyte Co-Localization at Electromagnetic Gap Hot-Spots for Highly Sensitive (Bio)Molecular Detection by Plasmon Enhanced Spectroscopies. *ACS Appl. Mater. Interfaces* **2021**, *13*, 9113−9121.

https://doi.org/10.1021/acsami.1c01953
ACS Appl. Mater. Interfaces 2021, 13, 32653−32661